

# Enhanced TM-Mode 3D Coupled Wave Theory for Photonic Crystal Surface-Emitting Terahertz Quantum Cascade Lasers

MINGXI CHEN,<sup>1,2,\*</sup> TSUNG-TSE LIN,<sup>1</sup> LI WANG,<sup>1</sup> HIDEKI HIRAYAMA,<sup>1</sup> AND  
CHIKO OTANI<sup>1,2,3</sup>

<sup>1</sup>*Terahertz-wave Research Group, RIKEN Center for Advanced Photonics, 519-1399 Aoba, Aramaki, Aoba-ku, Sendai, Miyagi 980-0845, Japan*

<sup>2</sup>*Department of Physics, Graduate School of Science, Tohoku University, 6-3 Aramaki Aza Aoba, Aoba-ku, Sendai 980-8578, Japan*

<sup>3</sup>[otani@riken.jp](mailto:otani@riken.jp)

[\\*mingxi.chen@riken.jp](mailto:mingxi.chen@riken.jp)

**Abstract:** In this study, we propose and develop an enhanced three-dimensional coupled wave theory (3D CWT) to investigate the optical field behavior in photonic crystal surface-emitting terahertz quantum cascade lasers (THz-QCLs). By incorporating an effective permittivity enhancement (EP) model and a self-consistent iteration (SCI) method, we successfully address the numerical dispersion issues encountered in analytical methods when dealing with metallic waveguide structures. The results demonstrate that the EP and SCI-enhanced 3D TM mode CWT achieves computational accuracy comparable to traditional numerical simulation methods such as finite-difference time-domain (FDTD), while significantly reducing the required computational resources, including time and memory, to just tens of minutes. Moreover, this method provides a clear physical insight, revealing the reasons behind the current low extraction efficiency in surface-emitting THz-QCLs. Our study showcases the potential of the EP and SCI-enhanced 3D CWT as a powerful simulation tool in the research of photonic crystal surface-emitting lasers, offering a new theoretical foundation and optimization direction for future laser designs.

## 1. Introduction

Terahertz quantum cascade lasers (THz-QCLs) have garnered significant attention due to their use of semiconductor superlattice structures in the conduction band, forming a series of potential wells, and achieving 1-5 THz band electrical injection laser radiation through electron transitions between these sublevels[1, 2]. As a compact, highly coherent, and energy-efficient THz source, THz-QCLs have shown immense application potential in various fields such as nondestructive testing, biological research, and high-speed communication[3-6]. Recently, THz-QCLs have successfully achieved a maximum output power exceeding 1 W and an operating temperature of 260 K[7-10], marking a significant step toward practical applications. However, due to the typical thickness of the active region (approximately 10  $\mu\text{m}$ )[11, 12] being much smaller than the wavelength of THz radiation in the air (about 100  $\mu\text{m}$ ), conventional edge-emitting THz-QCLs face severe diffraction issues, resulting in distorted far-field beam patterns[13, 14]. Moreover, current THz-QCLs struggle to achieve both high brightness and high operating temperatures simultaneously; most THz-QCLs only reach milliwatt-level brightness under near-room temperature conditions[9, 10, 15, 16]. Enhancing the far-field beam quality and radiation power has become a crucial challenge for the practical implementation of THz-QCLs.

Surface-emitting THz-QCLs with Guided Mode Resonance (GMR) photonic crystal structures offer unique advantages in addressing these challenges[17, 18]. Compared to traditional edge-emitting designs, surface-emitting lasers have a larger light extraction area, significantly improving the far-field mode and achieving higher radiation power. Additionally, due to the periodic spatial structure of the GMR photonic crystal, these lasers also achieve better single-mode operation. Similar method as [19, 20] is expected to apply to THz-QCLs, where

over the past decade, numerous studies have been conducted with the aim of achieving high-power surface-emitting THz-QCLs[21-23]. However, due to the limitations in light extraction efficiency from the waveguide structure, this goal has not yet been achieved. This remains a significant challenge in the research of surface-emitting THz-QCLs.

We believe that developing suitable simulation methods to gain a deeper understanding of the optical field behavior in photonic-crystal-structured surface emitting THz-QCLs is one of the important keys to addressing this challenge. Traditional numerical simulation methods, such as the Finite-Difference Time-Domain (FDTD) and Finite Element Method (FEM)[24, 25], although reliable, consume substantial computational resources, making it difficult to explore a large number of potential design schemes within a limited time[26, 27]. Besides, numerical methods only provide a surface-level understanding of the electromagnetic field distribution, lacking deep physical insights, thus making it challenging to quickly and clearly identify the specific reasons for the current low extraction efficiency of surface-emitting THz-QCLs.

Facing the similar challenges, recently, a new method called Three-Dimensional Coupled Wave Theory (3D CWT) has been applied and demonstrated in the infrared range for surface-emitting laser diodes and QCLs[26, 28, 29]. This method can quickly obtain information about vertical emitting lasers, including operating frequency, electromagnetic field intensity, and surface losses, with minimal resource consumption. As an analytical method, 3D CWT has unique advantages in explaining the sources and influencing factors of surface emissions.

We plan to utilize this powerful simulation method to analyze photonic-crystal-structured surface emitting THz-QCLs. However, in THz-QCLs, to maintain optical field confinement, metal waveguides must be introduced. The extreme permittivities of these materials present significant numerical dispersion issues for current 3D CWT calculations just like in FDTD[30]. To fully leverage this powerful analytical model and achieve high radiation power in photonic-crystal-structured surface emitting THz-QCLs, this study introduces the Effective Permittivity Enhancement (EP) model and the Self-Consistent Iteration (SCI) model to extend the 3D CWT for Transverse Magnetic (TM) polarization modes, making accurate simulation of THz-QCLs with metal waveguides possible. By comparing with the results of the FDTD method, we have verified the accuracy of this method and, for the first time, successfully revealed the reasons for the low extraction efficiency of current SE THz-QCLs compared to surface-emitting lasers in other bands using this analytical approach. Through this research, we also demonstrate the potential of the EP and SCI enhanced TM mode 3D CWT as an effective simulation tool for the study of photonic crystal surface-emitting lasers, including SE THz-QCLs.

## 2. Coupled Wave Theory Model

A typical photonic-crystal-structured surface emitting THz-QCLs structure[23, 31, 32] is shown in Figure 1. The optical field between waveguides exhibits different guided mode vertical distributions in the metal top layer and air node regions, resulting in different effective permittivities in various regions[32], as shown in Figure 3. By controlling the periodic distribution of the effective permittivities, photonic-crystal-structured surface emitting THz-QCLs can achieve efficient optical field control. Therefore, the kind of THz-QCLs are typical GMR photonic crystal devices. For GMR photonic crystals, when faced with large air nodes, strong permittivity contrasts, or complex photonic crystal structures, it has been reported that iterative optimization of the coupled wave theory is necessary to achieve sufficiently high simulation accuracy[33]. In this paper, we extend the SCI method to the TM mode 3D CWT, providing a robust simulation foundation.

However, the use of the SCI method alone is insufficient. The main difficulty in simulating photonic-crystal-structured surface emitting THz-QCLs using analytical methods arises from the extreme permittivities of metals. The significant difference between the permittivities of metals and semiconductors, reaching approximately three orders of magnitude, and the fact that the permittivities are complex with a negative real part in the THz band, describing strong optical field absorption by metals, pose additional challenges[30]. The abrupt change in the optical field at the metal-semiconductor interface can cause ringing artifacts, leading to severe

numerical dispersion (Figure 2.B). The extraordinary permittivities make it difficult for the self-consistent iteration method, commonly used under high refractive index contrast conditions between semiconductors, to guide numerical solutions towards true physical convergence.

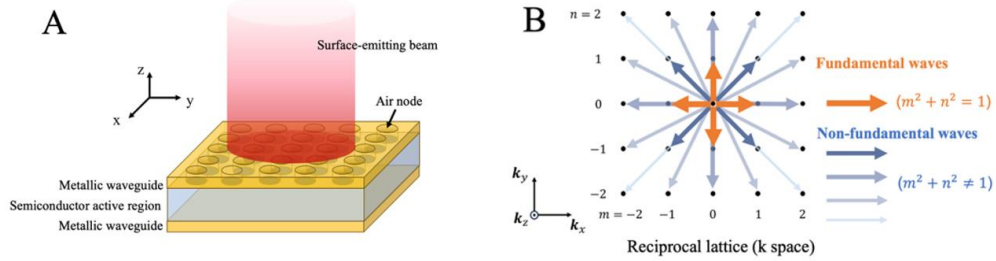


Fig. 1. A. The schematic depicts a typical structure of surface-emitting THz QCL with a two-dimensional GMR photonic crystal waveguide. Based on this structure, we will construct a CWT model. Here, we adopt a square lattice and neglect the ultrathin ( $\sim 50$  nm) heavily doped contact layer between the metal and the active region, which has a permittivity close to that of the metal. Assuming the device is sufficiently large to disregard the side boundary conditions, we can consider the device to be infinitely extended in the  $xy$ -plane. B. The reciprocal lattice corresponding to the photonic crystal, along with the wave vectors of the monochromatic Bloch waves.  $m, n$  are wavenumbers of each waves.

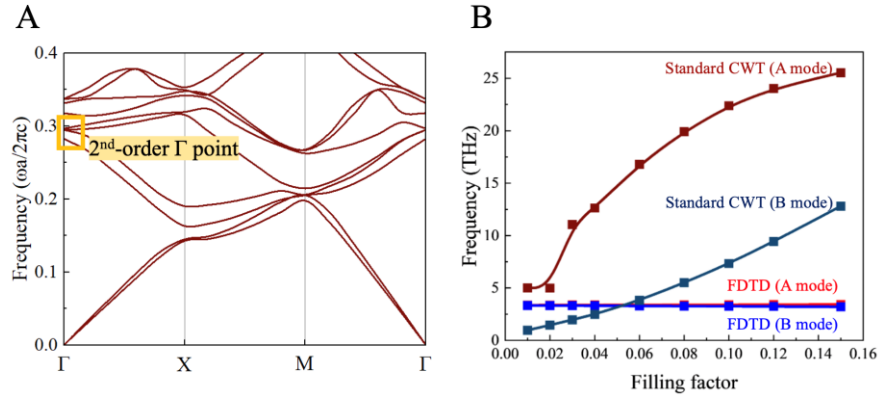


Fig. 2. A. We will focus on establishing a CWT model at the 2nd-order  $\Gamma$  point, as this point yields the highest surface emission efficiency. There are four supported sub-modes here, designated as A, B, and E ( $E_1, E_2$ ), which will be discussed in detail later. B. We observe that, due to the influence of the metal, using the standard CWT model alone can result in significant deviations from the relatively accurate values provided by FDTD simulations.

To bridge this significant numerical difference and extend the applicability of coupled wave theory to include plasmonic waveguides containing metals or heavily doped semiconductors, we introduce an effective permittivity enhancement algorithm. This algorithm avoids direct calculation of the metals, simplifying the problem to an equivalent model, thereby achieving high precision similar to that of coupled wave calculations conducted entirely on semiconductor devices. For clarity, the following sections will introduce the standard TM mode 3D CWT step by step and subsequently incorporate SCI and EP enhancements. To ensure clear and coherent derivation, the physical meanings of most symbols and notations required in the subsequent discussions are uniformly provided in Table 1.

**Table 1 Symbols used in derivation and their meanings.**

Symbol	Physical quantity
H	Magnetic field intensity
E	Electric field intensity

$\varepsilon(\mathbf{r})$	Permittivity (Permittivity) at space coordinates $\mathbf{r}$
$k$	Wave number
$k_0$	Resonant mode wave number
$\omega$	Angular frequency
$\omega_0$	Resonant mode angular frequency
$\beta_0$	Reciprocal unit cell size = $\frac{2\pi}{a(\text{unit size})}$
$H_{\alpha,mn}$	Bloch wave intensity with x and y wavenumbers equal to $m\beta_0$ and $n\beta_0$ along $\alpha$ direction
$\kappa_{mn}$	Fourier transform of the inverse permittivity
	$\varepsilon^{-1}(\mathbf{r}) = \sum_{mn} \kappa_{mn}(z) e^{-i\beta_0(mx+ny)}$
$\Theta(z)$	Vertical field distribution of fundamental waves
$A_{MN}$	Complex amplitude of fundamental waves
$\hat{K}_{mn}^{MN}$	Dispersion relation operator = $\kappa_{(M-m)(N-n)} \frac{\partial^2}{\partial z^2} + \left( \frac{\partial}{\partial z} \kappa_{(M-m)(N-n)} \right) \frac{\partial}{\partial z}$
$\hat{J}$	Dispersion relation operator = $\hat{K}_{mn}^{mn} + k_0^2 = \kappa_{00} \frac{\partial^2}{\partial z^2} + \left( \frac{\partial}{\partial z} \kappa_{00} \right) \frac{\partial}{\partial z} + k_0^2$

---

### 2.1 Standard TM-mode 3D CWT Mode

For the TM-mode optical field, the electric and magnetic fields can be expressed as  $\mathbf{E} = (0, 0, E_z)$  and  $\mathbf{H} = (H_x, H_y, 0)$  [29], respectively. To retain the polarization information of these fields, we choose the dispersion equation represented by the magnetic field  $\mathbf{H}$  as the starting point for our discussion, from the Faraday's law of electromagnetic induction and Ampère's law with Maxwell's correction, the master equation is given by

$$\nabla \times \left[ \frac{1}{\varepsilon(\mathbf{r})} \nabla \times \mathbf{H}(\mathbf{r}) \right] = k^2 \mathbf{H}(\mathbf{r}) \quad (1)$$

We select a laser with a multilayer thin-film structure, as shown in Figure 1, as the subject of our study. The two-dimensional photonic crystal is located in the x-y plane, while the multilayer structure extends along the z-axis. This is a typical structure for many surface-emitting lasers, including SE THz-QCLs. Considering the desire to reduce lateral mirror losses, improve surface emission brightness, and achieve smaller beam divergence angles and single-mode operation, photonic crystal surface-emitting lasers are typically designed with larger dimensions and more repeating units in the x-y direction. Therefore, assuming the device is infinite in the x-y direction with countless repeating periods and negligible horizontal losses is a reasonable approximation. Based on this discussion, we can fully utilize the periodicity in the x-y plane and apply the Bloch wave expansion to the above equation (i.e., Fourier transform). Thus, the magnetic field can be expanded as:

$$\mathbf{H}(\mathbf{r}) = \sum_{mn} e^{-i\beta_0(mx+ny)} \cdot \mathbf{H}_{mn}(z) = \sum_{mn} e^{-i\beta_0(mx+ny)} \cdot (H_{x,mn}, H_{y,mn}, 0) \quad (2)$$

Similarly, the inverse of the dielectric function can be expanded as:

$$\varepsilon^{-1}(\mathbf{r}) = \sum_{mn} \kappa_{mn}(z) e^{-i\beta_0(mx+ny)} \quad (3)$$

Substituting the above two equations into the dispersion equation, we obtain a set of equations describing the coupling relationships between various monochromatic frequency components in the x, y, and z directions:

$$\begin{aligned} & (\hat{J} - \beta_0^2 \kappa_{00} n'^2) H_{x,m'n'} + \beta_0^2 \kappa_{00} m' n' H_{y,m'n'} \\ & = \sum_{\substack{m \neq m' \\ n \neq n'}} \left[ \left( -\hat{K}_{mn}^{m'n'} + \beta_0^2 \kappa_{(m'-m)(n'-n)} n n' \right) H_{x,mn} - \beta_0^2 \kappa_{(m'-m)(n'-n)} m n' H_{y,mn} \right] \end{aligned} \quad (4)$$

$$\begin{aligned}
& (\hat{j} - \beta_0^2 \kappa_{00} m'^2) H_{y,m'n'} + \beta_0^2 \kappa_{00} m' n' H_{x,m'n'} \\
= & \sum_{\substack{m \neq m' \\ n \neq n'}} \left[ \left( -\hat{K}_{mn}^{m'n'} + \beta_0^2 \kappa_{(m'-m)(n'-n)} m m' \right) H_{y,mn} - \beta_0^2 \kappa_{(m'-m)(n'-n)} m' n H_{x,mn} \right] \quad (5)
\end{aligned}$$

$$\sum_{m,n} \kappa_{(m'-m)(n'-n)} \frac{\partial}{\partial z} (m' H_{x,mn} + n' H_{y,mn}) = 0 \quad (6)$$

We can categorize the various monochromatic waves present in the device based on the plane wave numbers into three groups: fundamental waves (FW), surface radiated waves (SR), and higher-order waves (HO). The wave number of the fundamental waves is  $\beta_{MN} = \sqrt{M^2 + N^2} \beta_0$ , satisfying  $\beta_{MN} \approx \omega_{act}/c$ , where  $\omega_{act}$  is the angular frequency of the radiation from the active region. Since the wave numbers of the fundamental waves are very close to the wave numbers of the radiation from the active layer, they will have the largest amplitude, dominating the optical field properties of the entire device. On the other hand, the plane wave number of the surface radiated waves is zero, meaning they can only propagate along the  $z$  direction, representing the components of surface radiation. Higher-order waves refer to other monochromatic wave components that are neither fundamental nor radiated waves. Intuitively, the closer the wave numbers of the fundamental and radiated waves, the higher the efficiency of generating surface radiation through coupling. Previous studies have also shown that the brightness of surface radiation in photonic crystal surface-emitting lasers can be written as:

$$B \propto \frac{S}{(M+1)(N+1)} \quad (7)$$

Evidently, at  $M^2 + N^2 = 1$ , near the 2nd- $\Gamma$  point of the photonic crystal band diagram, photonic crystal surface-emitting lasers exhibit the best light extraction efficiency. Therefore, in subsequent discussions, we will also consider the waves with  $M^2 + N^2 = 1$  as the fundamental waves.

In the resonant modes near the 2nd- $\Gamma$  point, the fundamental waves can be expressed as the product of the same longitudinal optical field distribution  $\Theta(z)$  and their respective complex amplitudes, specifically:

$$\begin{aligned}
H_{x,10} &= 0, & H_{y,10} &= A_{10} \Theta(z) \\
H_{x,-10} &= 0, & H_{y,-10} &= A_{-10} \Theta(z) \\
H_{x,10} &= A_{01} \Theta(z), & H_{y,10} &= 0 \\
H_{x,-10} &= A_{0-1} \Theta(z), & H_{y,-10} &= 0
\end{aligned} \quad (8)$$

Here,  $\Theta(z)$  can be obtained through the Transfer Matrix Method (TMM) on the waveguide with an averaged permittivity approximation (See. Supplemental Document), satisfying the following equation:

$$\left( \kappa_{00} \cdot \frac{\partial^2}{\partial z^2} + \frac{\partial}{\partial z} \kappa_{00} \cdot \frac{\partial}{\partial z} + k_0^2 - \beta_0^2 \kappa_{00} \right) \Theta(z) = 0 \quad (9)$$

Combining the above equations, we can obtain the following relationship:

$$\begin{aligned}
& k^2 A_{MN} = (k_0^2 + \delta_{FW} + \delta_{SR} + \delta_{HO}) A_{MN} \\
= & k_0^2 A_{MN} + \sum_{\substack{m \neq M \\ n \neq N}} \int dz \left\{ \Theta^* \cdot \left[ \begin{array}{c} -\hat{K}_{mn}^{MN} (N^2 H_{x,mn} + M^2 H_{y,mn}) \\ -\beta_0^2 \kappa_{(M-m)(N-n)} (M^3 - N^3) (n H_{x,mn} - m H_{y,mn}) \end{array} \right] \right\} \quad (10)
\end{aligned}$$

Note that here we have used the assumption  $M^2 + N^2 = 1$ . This equation describes a clear physical image: although the fundamental waves dominate the device behavior (the  $k_0^2 A_{MN}$  term on the right side of the equation), due to the presence of relatively weak non-fundamental waves, their coupling with the fundamental waves (the summation term on the right side of the equation) causes a shift in the working frequency  $k$  of the photonic crystal relative to the "clean" resonant mode  $k_0$ , with the magnitude of the shift attributed to  $\delta_{FW}$  (shift due to

coupling with fundamental waves),  $\delta_{SR}$  (shift due to coupling with surface radiated waves), and  $\delta_{HO}$  (shift due to coupling with higher-order waves).

The above discussion reveals a physical picture: in photonic crystal surface-emitting lasers, the intensities of monochromatic waves are not entirely independent due to their coupling relationships. Furthermore, the fundamental waves will dominate the electromagnetic field behavior throughout the device. Therefore, it naturally follows to expand the monochromatic waves using the four fundamental waves as a basis. This corresponds to a natural and clear physical process: in photonic crystal surface-emitting lasers, the fundamental waves are initially generated by the radiation from the active region, while other monochromatic wave components result from the coupling of fundamental waves as they propagate through the device:

$$H_{mn,\alpha} = T_{mn,\alpha}^{MN(1)} \cdot A_{MN} + T_{mn,\alpha}^{MN,M'N'(2)} \cdot A_{MN} \cdot A_{M'N'} + O^{(3)}(A_{MN}) \quad (\alpha = x, y) \quad (11)$$

For simplicity, Einstein summation notation is used here, with  $T$  being the expansion coefficient, and  $O^{(n)}$  representing the  $n^{\text{th}}$ -order small quantity. In the first-order approximation, Equation 10 can be transformed into an eigenvalue problem:

$$k^2 \mathbf{V} = \mathbf{C} \mathbf{V} = (k_0^2 + C_{FW} + C_{SR} + C_{HO}) \mathbf{V} \quad (12)$$

where,  $\mathbf{V} = (A_{10}, A_{-10}, A_{01}, A_{0-1})$  represents the complex amplitude vector of the fundamental waves. The specific form and derivation of the operator  $\mathbf{C}$  are provided in Supplemental Document.

## 2.2 SCI Model for Metal Photonic Crystals

When metals are present in Photonic crystal surface-emitting lasers, the standard CWT cannot effectively address the problem. This is because the high reflectivity of metals causes the electromagnetic field intensity to jump at the interface like a step function. When the electromagnetic field is expanded using Bloch waves under such conditions, it corresponds to components with frequencies much higher than those of the fundamental waves. For an ideal mirror, this would even correspond to infinitely high-frequency Bloch waves. Thus, the CWT model, which is based on the expansion of the electromagnetic field using a finite number of Bloch waves and focuses on the behavior of fundamental waves, cannot correctly simulate the behavior of devices with metal photonic crystal structures, such as photonic-crystal-structured surface emitting THz-QCLs.

Although the special electromagnetic field behavior introduced by metals makes direct standard CWT analysis challenging, the electromagnetic field penetrating the metal is extremely weak in practice, meaning that the presence or absence of metal mainly affects the regions outside the metal. We can describe this effect using an effective permittivity, which is the concept behind GMR photonic crystals. As shown in Figure 3, the effective permittivity allows us to construct an equivalent model for calculations, which we denoted as EP CWT, thus avoiding the difficulties of directly analyzing metal photonic crystals. The method for calculating the effective permittivity is based on guided mode obtained with transfer matrix method[34]. The details are provided in Supplemental Document A.

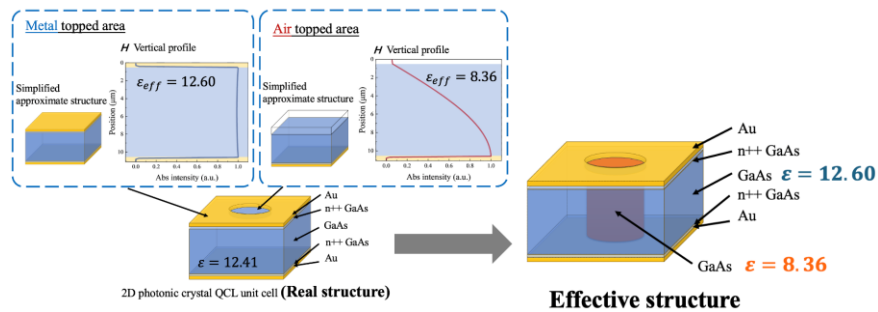


Fig. 3. The conceptual diagram of the EP CWT. By utilizing the effective permittivity obtained from different guided modes, we can transform the actual homogeneous GaAs active layer into an effective structure with varying permittivity. This approach allows us to incorporate the influence of the metal within the semiconductor layers, thus avoiding direct calculations involving the metal. Given the relatively mild differences in permittivity between semiconductors in the effective structure, we can expect high accuracy and rapid convergence in the calculations.

Through EP CWT, we avoid the difficulties of calculating near-infinite frequency components. However, the reflectivity of metals is so high that the differences in effective permittivity remain significant. Therefore, the amplitudes of higher-order waves are still relatively strong. When solving the working modes of Photonic crystal surface-emitting lasers containing metals using Equation 10, the term  $\mathbf{H}_{mn}$  on the right side of the equation cannot be simply regarded as the result of coupling only fundamental modes. To accurately solve for the amplitudes of the monochromatic waves  $\mathbf{H}_{mn}$ , we need to use Equations 4 and 5, considering the contributions of all modes  $\mathbf{H}_{m'n'}$  present in photonic crystal surface-emitting lasers. However, initially, we do not know the specific values of  $\mathbf{H}_{m'n'}$ .

This is why the traditional CWT model remains crucial: we can use the standard TM-mode CWT to provide a reasonable initial guess, then iteratively use the self-consistent iteration process, continually using the coupling output results of the previous round of electromagnetic field calculations as the input for the next round to solve Equations 4 and 5. This yields more accurate predictions of the Bloch wave intensities. This corresponds to a natural physical process: initially, only fundamental waves exist in photonic crystal surface-emitting lasers, which interact with each other and undergo reflection, refraction, and transmission at the medium interface, generating other frequency components. These newly generated electromagnetic waves also participate in the self-coupling process of the electromagnetic field until no new components are generated. At this point, the electromagnetic field has passed the relaxation time and reached a quasi-steady state. Computationally, this corresponds to finding a convergent solution. The flowchart of SCI CWT calculations is shown in Figure 4. The equations for updating  $\mathbf{H}_{mn}$  are provided in Supplemental Document.

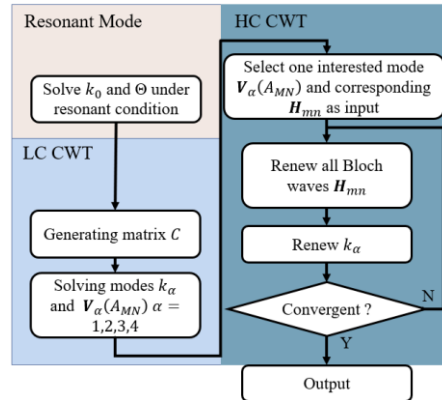


Fig. 4. Depicts the flowchart of TM mode CWT calculations. The program begins in the upper left corner and concludes in the lower right corner. It starts from zeroth-order mean field effects and proceeds through resonant mode calculations, LC-CWT calculations, and HC-CWT calculations. It is an iterative process from first-order perturbation to low-contrast approximation and finally to second-order-accuracy perturbation, involving higher-order-accuracy perturbations that provide quasi-exact solutions.

Finally, after a comprehensive review of the above derivations, we note that in the traditional TM-mode CWT model, the amplitudes of the monochromatic waves  $\mathbf{H}_{mn}$  are based on the first-order expansion of the fundamental mode amplitudes  $A_{MN}$ . Therefore, in the dispersion equation, the coupling of each monochromatic wave with the fundamental mode is

based on the first-order interaction of  $A_{MN}$  terms. This can be regarded as second-order perturbation theory concerning  $A_{MN}$ , i.e.,  $k^2 \approx k_0^2 + \lambda_1 O^{(1)}(A_{MN}) + \lambda_2 O^{(2)}(A_{MN})$ . Clearly, the SCI CWT solving process involves higher-order  $O^{(n)}(A_{MN})$ , and this iteration can be repeated multiple times until the desired accuracy is achieved. This method avoids the significant challenge of directly solving the amplitudes of hundreds of plane waves, constituting a semi-analytical approach.

### 3. Computational Results and Discussion

In this section, we present the computational results obtained from the enhanced 3D TM-mode CWT model, specifically for a typical SE THz QCL structure containing metallic photonic crystal waveguides. For comparison, we also utilized the traditional numerical method FDTD for simulating the same structure using OptiWave FDTD software. Due to the significant contrast between the semiconductor layers and the metallic material with a complex permittivity having a negative real part, the FDTD calculations tend to be unstable. Thus, we approximated the metal and the 50 nm thick contact layer as ideal conductors. Both the 3D TM-mode CWT and FDTD simulations employed identical periodic boundary conditions, and the actual calculation region size was one unit cell.

Additionally, we introduced the semi-analytical Plane Wave Expansion Method (PWEM) for comparison. Considering the structure is not periodic along the z-direction, performing full 3D PWEM calculations requires additional considerations. Here, we used its 2D form (2D PWEM) and applied the same effective permittivity approximation as in the CWT, treating the equivalent structure in PWEM calculations as the holes ( $\epsilon_{eff} \approx 8.375$ ) and the slab ( $\epsilon_{eff} \approx 12.602$ ). This is a reasonable and validated approximation for semiconductor devices.

First, we observed that all three methods correctly identified four supported sub-modes at the 2nd- $\Gamma$  point: two non-degenerate modes A and B, and two degenerate modes E1 and E2. The in-plane electric field distributions obtained from the CWT calculations are shown in Figure 5, with the patterns dependent on the symmetry of the unit cell and air nodes. The results are consistent with those from FDTD and PWEM.

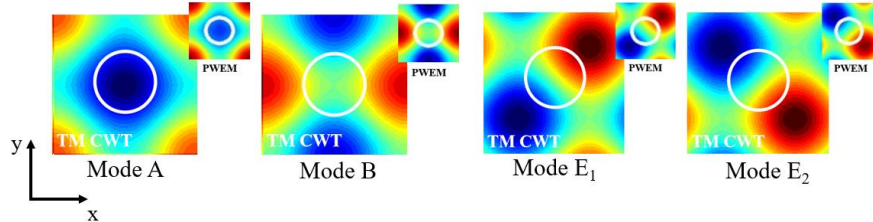


Fig. 5. In-plane  $E_z$  field patterns of antisymmetric (A, B) and symmetric (E) modes simulated by CWT and PWEM.

After confirming that the new CWT method correctly identified the four sub-modes, we proceeded to calculate the two primary factors of concern in PC SE THz QCL designs: operating frequency and surface emission efficiency. Firstly, regarding frequency, we varied the air node filling factor (filling factor = Air node area/unit cell area) between 0.01 and 0.15. We used a smaller upper limit for the air node size compared to infrared all-semiconductor surface-emitting lasers because excessive air node sizes have been reported to lead to device failure. This is understandable as QCLs require a high optical confinement factor to achieve emission, and the process of creating air nodes inevitably damages the microstructure of QCLs. The computational results are shown in Figures 6 and 7.

The results demonstrate excellent consistency between the new CWT method and the FDTD method across the computed parameter range for all three modes, with a maximum frequency deviation of only about 1% ( $\sim 0.03$  THz). Moreover, the SCI+EP enhanced 3D TM-mode CWT method showed significant accuracy advantages over the traditional semi-



analytical 2D PWEM method. This is because the 3D TM-mode CWT considers the behavior of electromagnetic waves along the z-direction, which is crucial for THz QCLs with high reflectivity waveguides. Additionally, we also have presented the results from the standard 3D TM-mode CWT without the SCI+EP enhancements in Figure 2B. As shown, the computation results diverged significantly due to the effects of the metal, further proving the necessity and correctness of introducing the new SCI+EP enhancement techniques when dealing with extreme permittivity materials.

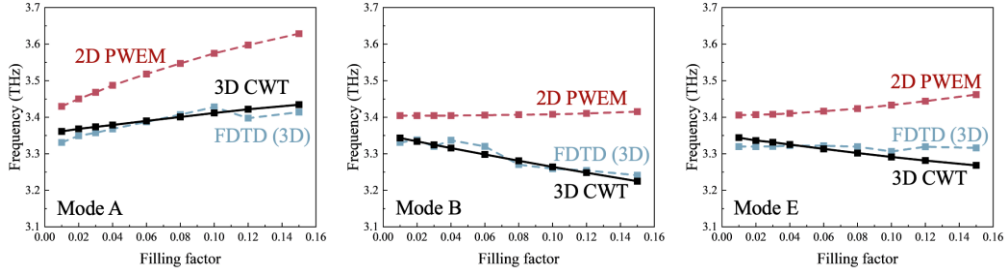


Fig. 6. Frequencies supported by photonic crystals predicted by CWT, FDTD and PWEM with varying air node filling factor from 0.01 to 0.15 for modes A, B and E.

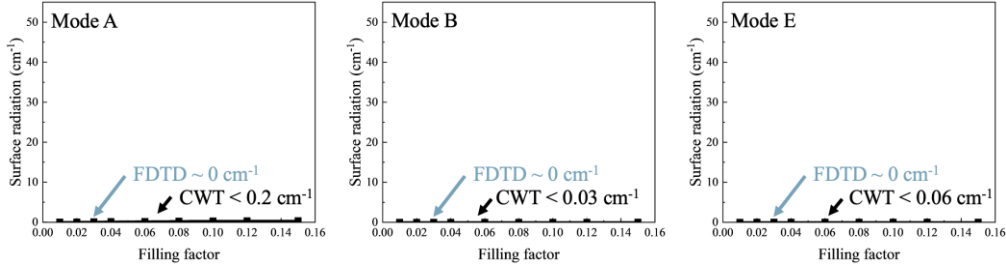


Fig. 7. Surface radiations supported by photonic crystals predicted by CWT and FDTD

Another critical aspect of PC SE THz QCL performance is its surface emission efficiency, where the 3D CWT method shows a distinct advantage over traditional analytical methods. Since we run full 3D simulations without requiring periodic structures along the z-direction, this method allows us to calculate energy emission efficiency along the z-direction. In contrast, PWEM requires periodicity in all calculation directions (or the introduction of superlattice structures or absorbing layers), making it challenging to compute surface emission efficiency using PWEM.

This time, we observed that unlike all-semiconductor photonic crystal surface-emitting lasers, both the FDTD and TM-mode CWT methods displayed surface emission efficiencies very close to 0 ( $< 0.2 \text{ cm}^{-1}$ ) regardless of the air node size variation. The good news is that once again, we verified the accuracy of the SCI+EP enhanced 3D TM-mode CWT results using the traditional and reliable FDTD method. However, unfortunately, the results indicate an inherent deficiency in surface emission performance for 2D photonic crystal waveguide structures utilizing the GMR effect. Considering that its surface radiation loss is lower than the typical lateral mirror loss of QCLs ( $\sim 4\text{-}20 \text{ cm}^{-1}$ ), SE QCLs without special treatment to obtain unique boundary conditions are prone to revert to lateral emission behavior. This conclusion aligns with earlier studies on surface-emitting QCLs and our group's experimental results. To date, all highly efficient surface-emitting THz QCLs have employed specialized structures to achieve high emission efficiency.

As a semi-analytical method, the 3D TM-mode CWT allows us to derive a clear physical image from the computation formulas, enabling us to directly understand the reasons behind the low emission efficiency of photonic crystal surface-emitting THz QCLs. This is something

that traditional FDTD methods cannot achieve. It may be the lack of intuitive insights into the problem's nature that has prevented the realization of high-power surface-emitting THz QCL structures similar to those in other wavelength ranges over the past 20 years, despite many efforts and significant discoveries.

By directly extracting the calculation formula related to surface emission, we see that:

$$I_{surf} \approx \int \left[ \Theta^*(z) \cdot \kappa(z) \frac{\partial^2}{\partial z^2} \left\{ \int dz' \left[ G(z, z') \kappa(z') \frac{\partial^2}{\partial z^2} \Theta(z') \right] \right\} \right] dz \propto \frac{\partial^2}{\partial z^2} \Theta(z) \quad (13)$$

The surface emission capability of the laser we are considering fundamentally arises from the uncertainty in the photon's momentum, specifically diffraction effects, represented by the second derivative term  $\frac{\partial^2}{\partial z^2} \Theta(z)$ . It is evident that plane waves propagating strictly in the horizontal direction struggle to achieve vertical components through certain sandwich-like GMR structures. A well-designed photonic crystal structure amplifies the z-component caused by diffraction, leading to notable surface emission. However, due to the high reflectivity of both the upper and lower waveguides, the upward and downward propagating components nearly cancel each other out, allowing only electromagnetic waves strictly confined to the horizontal direction, which making it naturally difficult to produce sufficient surface emission components. Note that we used ideal periodic boundary conditions for the calculations, so the finite scale structure may produce slightly higher surface emission efficiency due to imbalances in electromagnetic field distribution, but this does not affect our discussion results. Solutions to improve this issue will be detailed in our subsequent papers.

#### 4. Summary

This paper proposes and develops an enhanced TM-mode 3D CWT to address the numerical dispersion issues encountered in traditional analytical methods when dealing with waveguide structures made of metallic or metal-like materials. By incorporating an EP model and a SCI method, we significantly improved the computational accuracy and efficiency of 3D CWT in simulating photonic crystal surface-emitting THz-QCLs. Compared to traditional numerical simulation methods such as the FDTD method, our enhanced approach not only drastically reduces the computational resources required but also achieves similar accuracy within tens of minutes. In the case studies presented, the EP and SCI-enhanced 3D TM-mode CWT showed excellent agreement with the FDTD method in frequency calculations, with a maximum frequency deviation of only about 1% (~0.03 THz).

Over the past decade, surface-emitting THz-QCLs have faced the challenge of low extraction efficiency. Benefiting from the semi-analytical nature of CWT, the EP and SCI-enhanced 3D TM-mode CWT accurately reveals the reasons for the low extraction efficiency in current surface-emitting THz-QCLs: this is primarily due to the high reflectivity of the metallic waveguides, which causes the electromagnetic field intensity in the sub-wavelength thickness of the active layer to be highly symmetrical, leading to the cancellation of the upward and downward propagating components. Consequently, most of the electromagnetic waves strictly propagate along the xy-plane. This discovery provides a new theoretical foundation for understanding and optimizing SE THz-QCLs. Based on these findings, future work will focus on further optimizing the photonic crystal structures and surface-emitting conditions to achieve more efficient laser designs.

It is noteworthy that the methods presented in this paper are not limited to THz-QCLs but can also be widely applied to other photonic crystal surface-emitting lasers using metallic or metal-like waveguides, demonstrating potential in a broader range of applications. The EP and SCI-enhanced 3D CWT, as a powerful simulation tool, not only provides clear physical insights but also significantly improves computational efficiency, making it highly valuable for future laser design and optimization.

**Acknowledgment.** Mingxi Chen thanks the Junior Research Associate (JRA) program at RIKEN for supporting this work.

The authors declare no conflicts of interest.

## References

1. B. S. Williams, "Terahertz quantum-cascade lasers," *Nature photonics* **1**, 517-525 (2007).
2. H. Hirayama, W. Terashima, T.-T. Lin et al., "Recent progress and future prospects of THz quantum-cascade lasers," *Novel In-Plane Semiconductor Lasers XIV* **9382**, 157-167 (2015).
3. W. L. Chan, J. Deibel, and D. M. Mittleman, "Imaging with terahertz radiation," *Reports on progress in physics* **70**, 1325 (2007).
4. P. H. Siegel, "Terahertz technology," *IEEE Transactions on microwave theory and techniques* **50**, 910-928 (2002).
5. G. Scalari, C. Walther, M. Fischer et al., "THz and sub - THz quantum cascade lasers," *Laser & Photonics Reviews* **3**, 45-66 (2009).
6. Y. H. Tao, A. J. Fitzgerald, and V. P. Wallace, "Non-contact, non-destructive testing in various industrial sectors with terahertz technology," *Sensors* **20**, 712 (2020).
7. T.-T. Lin, L. Wang, K. Wang et al., "Over One Watt Output Power Terahertz Quantum Cascade Lasers by Using High Doping Concentration and Variable Barrier - Well Height," *physica status solidi (RRL) - Rapid Research Letters* **16**, 2200033 (2022).
8. L. Li, L. Chen, J. Freeman et al., "Multi - Watt high - power THz frequency quantum cascade lasers," *Electronics Letters* **53**, 799-800 (2017).
9. A. Khalatpour, A. K. Paulsen, C. Deimert et al., "High-power portable terahertz laser systems," *Nature Photonics* **15**, 16-20 (2021).
10. A. Khalatpour, M. C. Tam, S. J. Addamane et al., "Enhanced operating temperature in terahertz quantum cascade lasers based on direct phonon depopulation," *Applied Physics Letters* **122** (2023).
11. T. T. Lin, and H. Hirayama, "Variable Barrier height AlGaAs/GaAs quantum cascade laser operating at 3.7 THz," *physica status solidi (a)* **215**, 1700424 (2018).
12. A. M. Andrews, T. Zederbauer, H. Detz et al., "THz quantum cascade lasers," in *Molecular Beam Epitaxy*(Elsevier, 2018), pp. 597-624.
13. D. Shao, C. Yao, Z. Fu et al., "Terahertz quantum cascade lasers with sampled lateral gratings for single mode operation," *Frontiers of Optoelectronics* **14**, 94-98 (2021).
14. S. Fatholouloumi, E. Dupont, S. Razavipour et al., "Electrically switching transverse modes in high power THz quantum cascade lasers," *Optics express* **18**, 10036-10048 (2010).
15. T.-T. Lin, W. Terashima, and H. Hirayama, "250 mW output power operation of GaAs-based THz quantum cascade lasers," in *JSAP-OSA Joint Symposia*(Optica Publishing Group2017), p. 7a\_A409\_406.
16. A. Albo, and Q. Hu, "Investigating temperature degradation in THz quantum cascade lasers by examination of temperature dependence of output power," *Applied Physics Letters* **106** (2015).
17. G. Liang, E. Dupont, S. Fatholouloumi et al., "Planar integrated metasurfaces for highly-collimated terahertz quantum cascade lasers," *Scientific reports* **4**, 7083 (2014).
18. Y. Han, L. Li, J. Zhu et al., "Silver-based surface plasmon waveguide for terahertz quantum cascade lasers," *Optics express* **26**, 3814-3827 (2018).
19. T. Inoue, M. Yoshida, J. Gellera et al., "General recipe to realize photonic-crystal surface-emitting lasers with 100-W-to-1-kW single-mode operation," *Nature Communications* **13**, 3262 (2022).
20. S. Noda, K. Kitamura, T. Okino et al., "Photonic-crystal surface-emitting lasers: Review and introduction of modulated-photonic crystals," *IEEE Journal of Selected Topics in Quantum Electronics* **23**, 1-7 (2017).
21. J. Ryu, C. Sigler, C. Boyle et al., "Surface-emitting quantum cascade lasers with 2nd-order metal/semiconductor gratings for high continuous-wave performance," in *Novel In-Plane Semiconductor Lasers XIX*(SPIE2020), pp. 189-199.
22. Y. Jin, L. Gao, J. Chen et al., "High power surface emitting terahertz laser with hybrid second-and fourth-order Bragg gratings," *Nature communications* **9**, 1407 (2018).
23. O. P. Marshall, V. Apostolopoulos, J. R. Freeman et al., "Surface-emitting photonic crystal terahertz quantum cascade lasers," *Applied Physics Letters* **93**, 171112 (2008).
24. M. Yokoyama, and S. Noda, "Finite-difference time-domain simulation of two-dimensional photonic crystal surface-emitting laser," *Optics Express* **13**, 2869-2880 (2005).
25. R. Colombelli, K. Srinivasan, M. Troccoli et al., "Quantum cascade surface-emitting photonic crystal laser," *Science* **302**, 1374-1377 (2003).
26. C. Peng, Y. Liang, K. Sakai et al., "Coupled-wave analysis for photonic-crystal surface-emitting lasers on air holes with arbitrary sidewalls," *Optics Express* **19**, 24672-24686 (2011).
27. Y. Liang, C. Peng, K. Ishizaki et al., "Three-dimensional coupled-wave analysis for triangular-lattice photonic-crystal surface-emitting lasers with transverse-electric polarization," *Optics express* **21**, 565-580 (2013).
28. Y. Liang, C. Peng, K. Sakai et al., "Three-dimensional coupled-wave model for square-lattice photonic crystal lasers with transverse electric polarization: A general approach," *Physical Review B* **84**, 195119 (2011).

Preprint version uploaded to ArXiv. This version has not been peer-reviewed by Optica Publishing Group.

29. Y. Yang, C. Peng, Y. Liang et al., "Three-dimensional coupled-wave theory for the guided mode resonance in photonic crystal slabs: TM-like polarization," *Optics Letters* **39**, 4498-4501 (2014).
30. Y.-C. Liu, and K. Chang, "Simple implementation of effective permittivity at dispersive metal-dielectric tilt interfaces for open-source FDTD package," in *2013 USNC-URSI Radio Science Meeting (Joint with AP-S Symposium)*(IEEE2013), pp. 75-75.
31. L. Sirigu, R. Terazzi, M. I. Amanti et al., "Terahertz quantum cascade lasers based on two-dimensional photonic crystal resonators," *Optics Express* **16**, 5206-5217 (2008).
32. Y. Chassagneux, R. Colombelli, W. Maineult et al., "Electrically pumped photonic-crystal terahertz lasers controlled by boundary conditions," *Nature* **457**, 174-178 (2009).
33. Y. Yang, C. Peng, and Z. Li, "Semi-analytical approach for guided mode resonance in high-index-contrast photonic crystal slab: TE polarization," *Optics express* **21**, 20588-20600 (2013).
34. M. Vassell, "Structure of optical guided modes in planar multilayers of optically anisotropic materials," *JOSA* **64**, 166-173 (1974).